photonics

MDPI

Article

Partially Coherent Off-Axis Double Vortex Beam and Its Properties in Oceanic Turbulence

Luli Chen, Guiqiu Wang *, Yan Yin, Haiyang Zhong, Dajun Liu * and Yaochuan Wang

Department of Physics, College of Science, Dalian Maritime University, Dalian 116026, China
* Correspondence: gqwang@dlmu.edu.cn (G.W.); liudajun@dlmu.edu.cn (D.L.)

Abstract: A partially coherent off-axis double vortex beam (PCOADVB) composed of two off-axis vortices is theoretically presented. The analytical equations of a PCOADVB in oceanic turbulence are presented, and the intensity profiles and the number of coherence vortices of the PCOADVBs are investigated based on the derived expressions. The numerical results show that the intensity profiles of PCOADVBs are determined by the initial topological charges M_1 and M_2 and the positions of the off-axis vortices (x_{1d}, y_{1d}) and (x_{2d}, y_{2d}). The intensity profiles of PCOADVBs will lose the off-axis ring intensity profile and acquire a Gaussian-like profile as z increases, and stronger oceanic turbulence and a smaller σ can help the PCOADVB evolve into a spot with a Gaussian-like profile faster on propagation. The number of coherence vortices of a PCOADVB in oceanic turbulence will increase on propagation. The PCOADVB may have potential applications in underwater laser sensing and wireless communications.

Keywords: propagation; intensity; vortex beam; off-axis; partially coherent beam

1. Introduction

The studies of light waves in underwater environments are widely developed due to their applications in underwater wireless communication (UWC), and the evolutions of light waves in underwater environments are related to optical fields [1]. To view the propagation of light in underwater turbulence, the power spectrum was introduced to describe the refractive index fluctuations caused by the temperature, salinity, and rate of dissipation [2–4]. The power spectrum introduced by Li describes the unstable stratification turbulence [3]. Yao et al. introduced the wavelength into the power spectrum and proposed a new spectrum containing the temperature, salinity, and wavelength [4]. Using the power spectrum proposed by Nikishov et al. [2], Farwell and Korotkova theoretically studied the propagation properties, including the intensity and coherence of lasers in oceanic turbulence [5]. Based on the theory of coherence and polarization, Korotkova et al. analyzed the polarization properties of a stochastic beam in oceanic turbulence, and the findings showed that the evolution of polarization can be affected by the parameters of the initial beam and the environments [6]. Korotkova et al. analyzed the scintillation index of various beams propagating through weak oceanic turbulence based on the power spectrum, and the findings are useful for UWC [7]. Baykal investigated the scintillation index of a spherical wave in strong oceanic turbulence and analyzed the relationships between the index and oceanic parameters [8]. Wang et al. studied the influences of distance and oceanic parameters on the scintillation index and found that the plane wave was easily affected [9]. Considering the performances of the UWC links, Yousefi et al. viewed the propagation of a flat-topped beam array in a turbulent ocean and analyzed the influences of oceanic parameters on the bit error rate (BER) [10]. Ata et al. analyzed the influences of turbulence on BER based on the power spectrum of optical turbulence and examined the relationships between the UWC quality and oceanic parameters [11]. Based on the optical oceanic turbulence proposed by Yao et al. [4], the evolutions of the structure function and angle-of-arrival variance were

Citation: Chen, L.; Wang, G.; Yin, Y.; Zhong, H.; Liu, D.; Wang, Y. Partially Coherent Off-Axis Double Vortex Beam and Its Properties in Oceanic Turbulence. *Photonics* **2024**, *11*, 20. https://doi.org/10.3390/photonics11010020

Received: 23 November 2023
Revised: 6 December 2023
Accepted: 23 December 2023
Published: 26 December 2023

also discussed [12]. Liu et al. investigated the properties of a chirped Gaussian beam (CGB) in oceanic turbulence and discussed the effects of distance and oceanic parameters on the spectral shifts on propagation [13]. Jo et al. derived the analytical equations of a diffracted CGB in the ocean, showed the influences of a circular aperture on spectral properties, and found the spectral switch [14]. From previous work [15], one finds that partially coherent beams (PCBs) can reduce the negative effects of atmospheric turbulence. So far, the properties of the PCBs in oceanic turbulence have been discussed [16–21]. Wu et al. derived the expressions of a Gaussian-Schell model (GSM) beam in oceanic turbulence and found that the beam wander can be affected by the source parameters and the ocean [16]. Lu and Zhao derived the expressions of a cusped random beam in oceanic turbulence, analyzed the propagation properties (intensity and coherence), and found that the intensity pattern can be destroyed by strong turbulence [17]. Chen and Zhao proposed an electromagnetic rectangular multi-GSM beam, studied the properties of this rectangular multi-GSM beam in oceanic turbulence, and found that the rectangular profiles became less flat as the distance increased [18]. Zhou et al. derived the analytical equations of a multi-sinc correlation beam in an anisotropic turbulent ocean and investigated the evolutions of the lattice intensity profile on propagation [19]. Liu et al. analyzed the propagation of a twisted GSM beam through a turbulent ocean and found that the rotation direction of a twisted GSM beam was not affected on propagation [20]. Liu et al. investigated the second-order statistics of a Hermite-GSM beam in oceanic turbulence and found that the splitting properties can be destroyed by turbulence and that the beams became a spot with the Gaussian profile [21]. On the other hand, array beams in underwater turbulence have also been widely analyzed. Luo et al. derived the expressions of an optical coherence lattice (OCL) in a turbulent ocean and found that the intensity at the receiver can be increased by controlling the initial beam parameters [22]. Ye et al. introduced a model of a rotating elliptical OCL in a turbulent ocean, studied the evolution of its properties, and showed that the rotation directions of the sub-beams can be maintained [23]. Liu et al. introduced a model of a phased locked multi-GSM beam array, derived the equations in oceanic turbulence, investigated the effects of oceanic turbulence on the beam's properties, and found that the sub-beam can have a flatter profile and that the intensity profiles can have a more Gaussian profile as the distance increases [24]. In addition, the vortex beams in oceanic turbulence have been extensively studied. Huang et al. proposed a model of a GSM vortex beam in a turbulent ocean and investigated the properties of such a beam [25]. Liu et al. extended an anomalous vortex beam (AVB) to a partially coherent AVB and studied the properties of such a beam in oceanic turbulence [26]. Wang et al. introduced a model of an off-axis GSM vortex beam in an anisotropic turbulent ocean and investigated the influences of oceanic parameters on intensity profiles [27].

Recently, beams with a double vortex (DV) and their properties were presented. Fang and Pu proposed the expression of stochastic coaxial DV beams correlated with a GSM source, derived the equations of this beam in the atmosphere, and analyzed the evolution of polarization [28]. Fang et al. introduced a new fractional DV beam consisting of two coaxial fractional topological charges, and this fractional DV beam was experimentally generated [29]. Liu et al. introduced a model of coaxial DV beams in atmospheric turbulence, analyzed the scintillation index, and found that the scintillation indices became smaller than the Gaussian beam [30]. Du et al. theoretically proposed the double-ring perfect vortex beam, and the perfect DV beam was experimentally generated using SLM [31]. Rickenstorff et al. investigated the tightly focused properties of perfect DV beams [32]. Based on the method of superposition, Ke and Zhang experimentally generated DV beams [33]. Guo et al. investigated the generation of off-axis DV beams [34]. Meanwhile, the laser arrays with a vortex can also be realized [35]. Moreover, the vortex beam can also be generated by metasurfaces [36,37]. Hence, these studies show that the DV beam is an important research topic.

The properties of DV beams can be controlled by topological charges and off-axis positions, and such beams have special intensity profiles [28–32]. The PCBs are well-liked in turbulent environments. In this work, we identify a beam with double vortices as a topic of interest, extend the off-axis double vortex beam (OADVB) with two vortices into the partially coherent OADVB (PCOADVB) correlated with a GSM source, focus on the evolutions of PCOADVBs, and investigate the intensity and coherence of the vortices of PCAODVBs in oceanic turbulence on propagation. In Section 2, we present the cross-spectral density (CSD) of a PCOADVB correlated with a GSM source. In Section 3, we derive the propagation CSD of a PCOADVB in oceanic turbulence based on the generalized Huygens–Fresnel integral. In Section 4, we show the intensity profiles and number of coherence vortices of a PCOADVB by employing the numerical results. In Section 5, the conclusion of this work is summarized.

2. Theoretical Model of a PCOADVB

In the Cartesian coordinate system, the expression of an OADVB at $z = 0$ is expressed as [34]

$$E(\mathbf{r},0) = \exp\left(-\frac{\mathbf{r}^2}{w_0^2}\right)[(x-x_{1d})+i(y-y_{1d})]^{M_1}[(x-x_{2d})+i(y-y_{2d})]^{M_2} \tag{1}$$

where $E(\mathbf{r})$ is the electric field; $\mathbf{r} \equiv (x,y)$ is the position vector; w_0 is the beam waist; $M_j(j=1,2)$ is the topological charge; and (x_{jd},y_{jd}) is the position of the off-axis vortex.

Considering a beam propagating along the z-axis and recalling the theory of coherence [38], the CSD of a PCB is written as

$$W(\mathbf{r}_1,\mathbf{r}_2,0) = \langle E(\mathbf{r}_1,0)E^*(\mathbf{r}_2,0)\rangle \tag{2}$$

In Equation (2), the $*$ represents the complex conjugate.

Substituting Equation (1) into Equation (2), the CSD of a PCOADVB correlated with a GSM source at $z=0$ can be obtained as

$$\begin{aligned} W(\mathbf{r}_1,\mathbf{r}_2,0) = \ & \exp\left(-\frac{\mathbf{r}_1^2+\mathbf{r}_2^2}{w_0^2}\right)[(x_1-x_{1d})+i(y_1-y_{1d})]^{M_1}[(x_1-x_{2d})+i(y_1-y_{2d})]^{M_2} \\ & [(x_2-x_{1d})-i(y_2-y_{1d})]^{M_1}[(x_2-x_{2d})-i(y_2-y_{2d})]^{M_2}\exp\left[-\frac{(x_1-x_2)^2}{2\sigma_x^2}-\frac{(y_1-y_2)^2}{2\sigma_y^2}\right] \end{aligned} \tag{3}$$

where $\sigma_\beta(\beta = x,y)$ is the coherence length in Equation (3).

3. Propagation CSD of a PCOADVB in Oceanic Turbulence

When a PCOADVB propagates along the z-axis, recalling the generalized Huygens–Fresnel integral, the expression of a PCOADVB in oceanic turbulence is given as [16–26]:

$$\begin{aligned} W(\boldsymbol{\rho}_1,\boldsymbol{\rho}_2,z) = \ & \frac{k^2}{4\pi^2z^2}\int_{-\infty}^{+\infty}\int_{-\infty}^{+\infty}\int_{-\infty}^{+\infty}\int_{-\infty}^{+\infty}W(\mathbf{r}_1,\mathbf{r}_2,0) \\ & \times\exp\left[-\frac{ik}{2z}(\boldsymbol{\rho}_1-\mathbf{r}_1)^2+\frac{ik}{2z}(\boldsymbol{\rho}_2-\mathbf{r}_2)^2\right]\langle\exp[\psi(\mathbf{r}_1,\boldsymbol{\rho}_1)+\psi^*(\mathbf{r}_2,\boldsymbol{\rho}_2)]\rangle d\mathbf{r}_1 d\mathbf{r}_2 \end{aligned} \tag{4}$$

where $\boldsymbol{\rho} \equiv (\rho_x,\rho_y)$ is the position vector at position z. $k = 2\pi/\lambda$ is the wavenumber, and λ denotes wavelength. $\psi(\mathbf{r}_0,\mathbf{r})$ is the phase perturbation in oceanic turbulence, and

$$\langle\exp[\psi(\mathbf{r}_1,\boldsymbol{\rho}_1)+\psi^*(\mathbf{r}_2,\boldsymbol{\rho}_2)]\rangle = \exp\left[-\frac{(\mathbf{r}_1-\mathbf{r}_2)^2+(\mathbf{r}_1-\mathbf{r}_2)(\boldsymbol{\rho}_1-\boldsymbol{\rho}_2)+(\boldsymbol{\rho}_1-\boldsymbol{\rho}_2)^2}{\Lambda_0^2}\right] \tag{5}$$

$$\Lambda_0^2 = 3/\pi^2k^2z\int_0^\infty d\kappa\kappa^3\Phi(\kappa). \tag{6}$$

In Equation (6), the power spectrum $\Phi(\kappa)$ can be written as [2]

$$\Phi(\kappa) = 0.388\times 10^{-8}\varepsilon^{-1/3}\kappa^{-11/3}\frac{\chi_T}{\varsigma^2}\left[1+2.35(\kappa\eta)^{2/3}\right]\left[\varsigma^2\exp(-A_T\delta)+\exp(-A_S\delta)-2\varsigma\exp(-A_{TS}\delta)\right] \tag{7}$$

where κ is the spatial frequency. The parameters A_T, A_S, and A_{TS} of seawater are set as 1.863×10^{-2}, 1.9×10^{-4}, and 9.41×10^{-3}, respectively; $\delta = 8.284(\kappa\eta)^{4/3}+12.978(\kappa\eta)^2$ [2]; χ_T corresponds with mean squared temperature; ε corresponds with the dissipation of turbulent kinetic energy; ς corresponds with the ratio of temperature to salinity. η represents the inner scale [2].

Recall the following equations [39]:

$$(x+y)^l = \sum_{h=0}^{l}\frac{l!}{h!(l-h)!}x^{l-h}y^h \tag{8}$$

$$\int_{-\infty}^{+\infty} x^n\exp\left(-ax^2+2bx\right)dx = n!\exp\left(\frac{q^2}{p}\right)\left(\frac{q}{p}\right)^n\sqrt{\frac{\pi}{p}}\sum_{l=0}^{[\frac{n}{2}]}\frac{1}{l!(n-2l)!}\left(\frac{p}{4q^2}\right)^l \tag{9}$$

$$H_n(x) = \sum_{l=0}^{[\frac{n}{2}]}\frac{(-1)^l n!}{l!(n-2l)!}(2x)^{n-2l} \tag{10}$$

Substituting Equation (3) into Equation (4), the CSD of a PCOADVB in oceanic turbulence at z is derived as

$$\begin{aligned} W(\boldsymbol{\rho}_1,\boldsymbol{\rho}_2,z) &= \tfrac{k^2}{4\pi^2z^2}\exp\left[-\tfrac{ik}{2z}\left(\boldsymbol{\rho}_1^2-\boldsymbol{\rho}_2^2\right)\right]\exp\left[-\tfrac{(\rho_{1x}-\rho_{2x})^2+(\rho_{1y}-y_{2y})^2}{\Lambda_0^2}\right] \\ &\sum_{s_1=0}^{M_1}\tfrac{M_1!(-1)^{M_1-s_1}}{s_1!(M_1-s_1)!}(x_{1d}+iy_{1d})^{M_1-s_1}\sum_{s_2=0}^{M_2}\tfrac{M_2!(-1)^{M_2-s_2}}{s_s!(M_2-s_2)!}(x_{2d}+iy_{2d})^{M_2-s_2} \\ &\sum_{s_3=0}^{M_1}\tfrac{M_1!(-1)^{M_1-s_3}}{s_3!(M_1-s_3)!}(x_{1d}+iy_{1d})^{M_1-s_3}\sum_{s_4=0}^{M_2}\tfrac{M_2!(-1)^{M_2-s_4}}{s_4!(M_2-s_4)!}(x_{2d}+iy_{2d})^{M_2-s_4} \\ &\sum_{l=0}^{s_1+s_2}\tfrac{(s_1+s_2)!i^l}{l!(s_1+s_2-l)!}\sum_{m=0}^{s_3+s_4}\tfrac{(s_3+s_4)!(-i)^m}{m!(s_3+s_4-m)!}W(\rho_x,z)W(\rho_y,z) \end{aligned} \tag{11}$$

where

$$\begin{aligned} W(\rho_x,z) = &\sqrt{\tfrac{\pi}{a_x}}(s_1+s_2-l)!\left(\tfrac{1}{a_x}\right)^{s_1+s_2-l}\sum_{s=0}^{[\frac{s_1+s_2-l}{2}]}\tfrac{1}{s!(s_1+s_2-l-2s)!}\left(\tfrac{a_x}{4}\right)^s\exp\left[\tfrac{1}{a_x}\left(\tfrac{ik}{2z}\rho_{1x}-\tfrac{\rho_{1x}-\rho_{2x}}{2\Lambda_0^2}\right)^2\right] \\ &\sum_{t=0}^{s_1+s_2-l-2s}\tfrac{(s_1+s_2-l-2s)!}{t!(s_1+s_2-l-2s-t)!}\left(\tfrac{ik}{2z}\rho_{1x}-\tfrac{\rho_{1x}-\rho_{2x}}{2\Lambda_0^2}\right)^{s_1+s_2-l-2s-t}\left(\tfrac{1}{\sigma_x^2}+\tfrac{1}{\Lambda_0^2}\right)^t\sqrt{\tfrac{\pi}{b_x}}\left(\tfrac{i}{2\sqrt{b_x}}\right)^{(s_3+s_4-m+t)}\exp\left(\tfrac{c_x^2}{b_x}\right)H_{s_3+s_4-m+t}\left(-\tfrac{ic_x}{\sqrt{b_x}}\right) \end{aligned} \tag{12}$$

$$\begin{aligned} W(\rho_y,z) = &\sqrt{\tfrac{\pi}{a_y}}l!\left(\tfrac{1}{a_y}\right)^l\sum_{s=0}^{[\frac{l}{2}]}\tfrac{1}{s!(l-2s)!}\left(\tfrac{a_y}{4}\right)^s\exp\left[\tfrac{1}{a_y}\left(\tfrac{ik}{2z}\rho_{1y}-\tfrac{\rho_{1y}-\rho_{2y}}{2\Lambda_0^2}\right)^2\right] \\ &\sum_{t=0}^{l-2s}\tfrac{(l-2s)!}{t!(l-2s-t)!}\left(\tfrac{ik}{2z}\rho_{1y}-\tfrac{\rho_{1y}-\rho_{2y}}{2\Lambda_0^2}\right)^{l-2s-t}\left(\tfrac{1}{2\sigma_y^2}+\tfrac{1}{\Lambda_0^2}\right)^t\sqrt{\tfrac{\pi}{b_y}}\left(\tfrac{i}{2\sqrt{b_y}}\right)^{m+t}\exp\left(\tfrac{c_y^2}{b_y}\right)H_{m+t}\left(-\tfrac{ic_y}{\sqrt{b_y}}\right) \end{aligned} \tag{13}$$

with

$$a_\beta = \frac{1}{w_0^2}+\frac{1}{2\sigma_\beta^2}+\frac{1}{\Lambda_0^2}+\frac{ik}{2z}(\beta = x,y) \tag{14}$$

$$b_\beta = \frac{1}{w_0^2}+\frac{1}{2\sigma_\beta^2}+\frac{1}{\Lambda_0^2}-\frac{ik}{2z}-\frac{1}{a_\beta}\left(\frac{1}{2\sigma_\beta^2}+\frac{1}{\Lambda_0^2}\right)^2 \tag{15}$$

$$c_\beta = \frac{1}{a_\beta}\left(\frac{ik}{2z}\rho_{1\beta} - \frac{\rho_{1\beta}-\rho_{2\beta}}{2\Lambda_0^2}\right)\left(\frac{1}{2\sigma_\beta^2}+\frac{1}{\Lambda_0^2}\right) - \frac{ik}{2z}\rho_{2\beta} + \frac{\rho_{1\beta}-\rho_{2\beta}}{2\Lambda_0^2}. \tag{16}$$

Equations (11)–(16) are the derived CSD of a PCOADVB. By using the above expressions, the propagation properties can be analyzed. When $\Lambda_0 = \inf$, the expressions of a PCOADVB will reduce to the CSD in free space.

When $\boldsymbol{\rho}_1 = \boldsymbol{\rho}_2 = \boldsymbol{\rho}$, the intensity of a PCOADVB in oceanic turbulence at the receiver plane is expressed as [36]

$$S(\boldsymbol{\rho}, z) = W(\boldsymbol{\rho}, \boldsymbol{\rho}, z). \tag{17}$$

The coherence of a PCOADVB in oceanic turbulence at points $\boldsymbol{\rho}_1 = (\rho_{1x}, \rho_{1y})$ and $\boldsymbol{\rho}_2 = (\rho_{2x}, \rho_{2y})$ can be presented as [38]:

$$\mu(\boldsymbol{\rho}_1, \boldsymbol{\rho}_2, z) = \frac{W(\boldsymbol{\rho}_1, \boldsymbol{\rho}_2, z)}{\sqrt{S(\boldsymbol{\rho}_1, z)S(\boldsymbol{\rho}_2, z)}}. \tag{18}$$

The position of the coherence vortices for a PCOADVB in oceanic turbulence at z is given as [40]

$$\mathrm{Re}[\mu(\boldsymbol{\rho}_1, \boldsymbol{\rho}_2, z)] = 0 \tag{19}$$

$$\mathrm{Im}[\mu(\boldsymbol{\rho}_1, \boldsymbol{\rho}_2, z)] = 0 \tag{20}$$

where $\mathrm{Re}[\mu(\boldsymbol{\rho}_1, \boldsymbol{\rho}_2, z)]$ is the real part and $\mathrm{Im}[\mu(\boldsymbol{\rho}_1, \boldsymbol{\rho}_2, z)]$ is the imaginary part.

4. Numerical Results and Discussions

Here, the intensity profiles and coherence vortices of a PCOADVB are investigated using the derived equations, and the relationships between properties (intensity and number of coherence vortices) with parameters that include beam and oceanic turbulence are discussed. In numerical examples, the parameters are taken as $\lambda = 417$nm, $w_0 = 2$ mm, $\sigma_x = \sigma_y = \sigma$, $M_1 = M_2 = 1$, $\varsigma = -2.5$, $\varepsilon = 10^{-7}$ m^2/s^3, and $\eta = 1$ mm without being shown in the figures.

First, the intensity profiles of a PCOADVB in free space ($\Lambda_0 = \inf$) are analyzed using Equation (17). Figure 1 illustrates the intensity distributions of a PCOADVB with $(x_{1d}, y_{1d}) = (1\text{ mm}, 0)$, $(x_{2d}, y_{2d}) = (0, 1\text{ mm})$, and $\sigma = 2$ mm in free space. From Figure 1a, one sees that the intensity profile of a PCOADVB has a dark ring accompanied by a bright spot pattern at $z = 10$ m, while the vortex beam has a circular-ring pattern with a dark center [25]. Thus, the off-axis ring intensity profile is caused by the off-axis position. The off-axis intensity profiles were viewed in the previous off-axis GSM vortex beam [27]. However, the off-axis profiles here are introduced by two off-axis positions: (x_{jd}, y_{jd}). As z increases to $z = 40$ m, the dark ring of a PCOADVB becomes smaller (Figure 1b). As z increases further, the intensity profile evolves into one spot (Figure 1c). When the distance is large enough, the off-axis ring distribution will become an off-axis Gaussian-like profile at $z = 200$ m (Figure 1d). To view the effects of σ on the off-axis ring intensity profile on propagation, the intensity profiles of the OADVB ($\sigma = \inf$) with the different off-axis positions (x_{jd}, y_{jd}) at $z = 200$ m in free space are shown in Figure 2. From Figure 2a, it was found that the off-axis ring intensity profile of an OADVB in free space will continue to have an off-axis ring-like profile, while the profiles of a PCOADVB become one spot pattern at $z = 200$ m (Figure 1d). Comparing Figure 1d with Figure 2a, one concludes that the one spot with an off-axis Gaussian-like profile of a PCOADVB at $z = 200$ m is caused by σ. The observation that the off-axis intensity profile becomes one spot is also viewed in the off-axis GSM vortex beam, which can be explained as an effect of σ [27]. When the two off-axis positions (x_{jd}, y_{jd}) of an OADVB change to $(x_{1d}, y_{1d}) = (1\text{mm}, 0)$ and $(x_{2d}, y_{2d}) = (-1\text{ mm}, 0)$, as depicted in Figure 2b, one finds that the off-axis ring intensity profile can have two hollow rings accompanied by two spots. The intensity profile of an OADVB in free space will evolve as the two off-axis positions (x_{jd}, y_{jd}) change. Thus, the intensity profiles of an OADVB can be controlled by modulating (x_{1d}, y_{1d}) and (x_{2d}, y_{2d}).

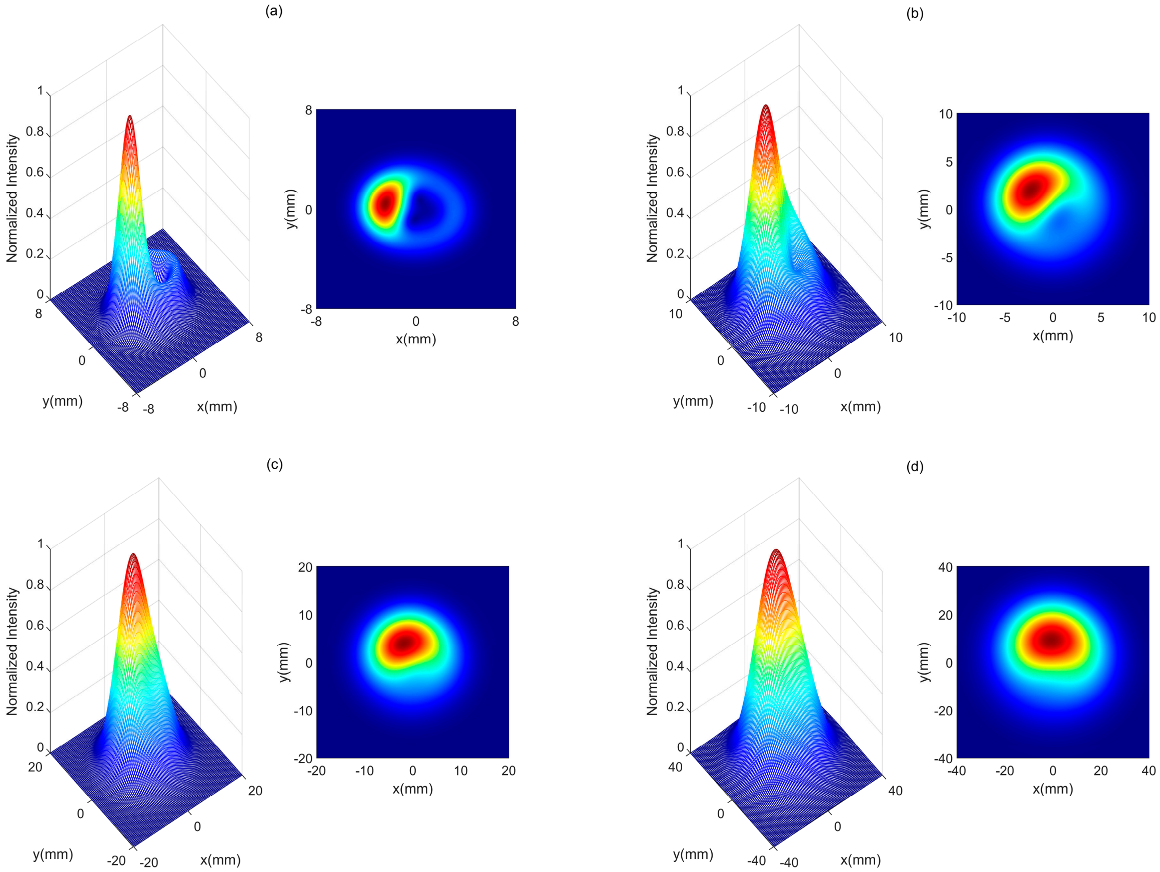

Figure 1. The intensity of a PCOADVB with $\sigma = 2$ mm in free space. (**a**) $z = 10$ m, (**b**) $z = 40$ m, (**c**) $z = 80$ m, and (**d**) $z = 200$ m.

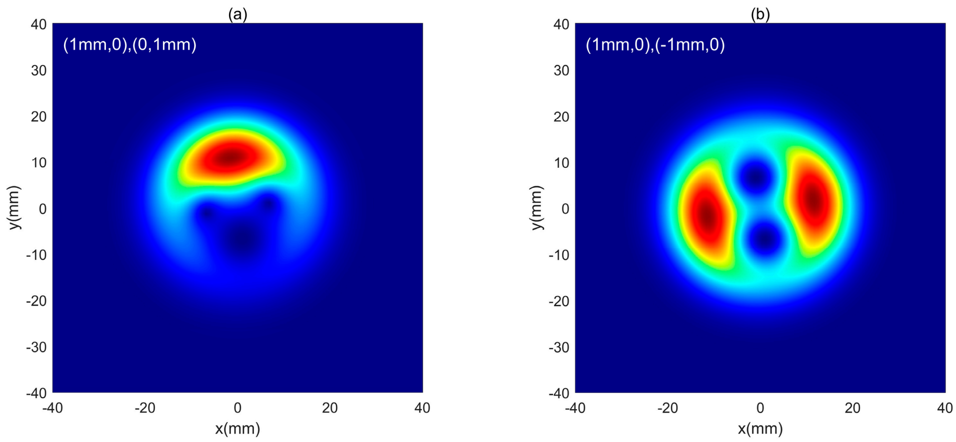

Figure 2. The intensity of an OADVB in free space at $z = 200$ m.

The expression of the CSD of a PCOADVB contains the off-axis position (x_{jd}, y_{jd}); thus, the intensity profiles may evolve when the off-axis positions change. The effects of the two off-axis positions (x_{jd}, y_{jd}) on the intensity profiles of a PCOADVB on propagation were analyzed. Figure 3 shows the intensity profiles of a PCOADVB with $(x_{1d}, y_{1d}) = (1\ \text{mm}, 0)$, $(x_{2d}, y_{2d}) = (-1\ \text{mm}, 0)$, and $\sigma = 2$ mm in free space. From Figure 3a, one sees that the intensity profile of a PCOADVB has an elliptical ring profile with a dark center at $z = 10$ m, while the intensity profile of a PCOADVB in Figure 1a has an off-axis ring pattern. Comparing Figure 1a with Figure 3a, it was concluded that the off-axis ring intensity profile of a PCOADVB can be realized by setting the off-axis positions (x_{jd}, y_{jd})

at $z = 10$ m, and the intensity profiles of a PCOADVB can be modulated by setting the off-axis position. As z increases to $z = 40$ m, the elliptical ring pattern evolves into one spot with two peaks (Figure 3b). As z increases further, this intensity profile gradually becomes one spot with a Gaussian-like profile at $z = 200$ m (Figure 3d), while the intensity profile of an OADVB with $(x_{1d}, y_{1d}) = (1\text{ mm}, 0)$ and $(x_{2d}, y_{2d}) = (-1\text{ mm}, 0)$ in free space remains two hollow rings accompanied by two spots at $z = 200$ m (Figure 2b). Thus, the spot pattern found in Figure 3d is introduced by $\sigma = 2$ mm. Comparing Figure 1d with Figure 3d, the center of the Gaussian-like spot has a different center when the off-axis positions change. From Figures 1–3, one concludes that the σ will help the PCOADVB evolve into a Gaussian-like beam on propagation.

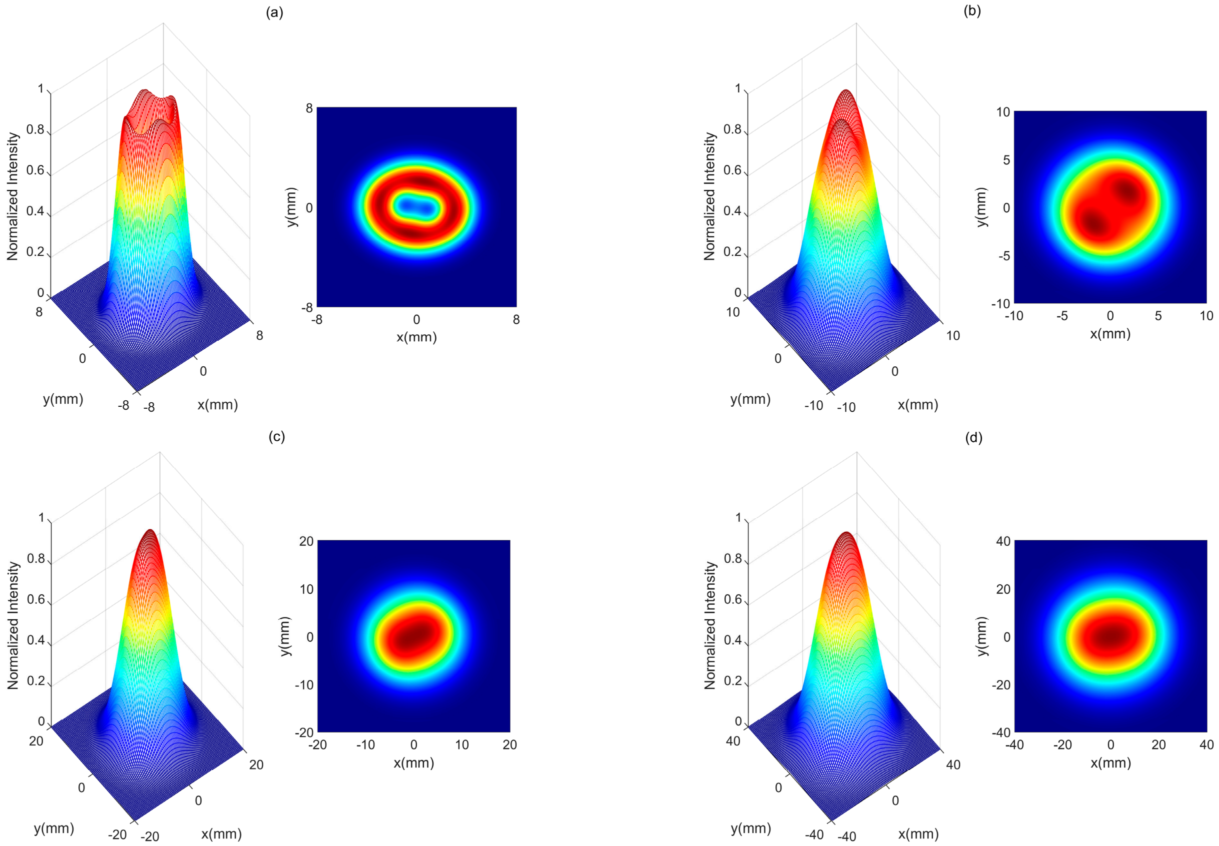

Figure 3. The intensity of a PCOADVB with $(x_{1d}, y_{1d}) = (1\text{ mm}, 0)$ and $(x_{2d}, y_{2d}) = (-1\text{ mm}, 0)$ in free space. (**a**) $z = 10$ m, (**b**) $z = 40$ m, (**c**) $z = 80$ m, and (**d**) $z = 200$ m.

Next, the relationships between the two topological charges M_1 and M_2 with the intensity pattern of a PCOADVB in free space were investigated. Figures 4 and 5 present the intensity profiles of a PCOADVB with $(x_{1d}, y_{1d}) = (1\text{ mm}, 0)$ and $(x_{2d}, y_{2d}) = (-1\text{ mm}, 0)$ (with $\sigma = 2$ mm) for the different topological charges M_1 and M_2, respectively. In Figure 4a, the intensity profile of a PCOADVB with $M_1 = 2$ and $M_2 = 1$ has an elliptical ring profile accompanied by a bright spot on the left at $z = 10$ m, and the intensity of the elliptical ring on the right is weak, while the intensity profile of the PCOADVB with $M_1 = M_2 = 1$ has an elliptical ring pattern at $z = 10$ m (Figure 3a). Comparing Figure 3a with Figure 4a, the differences in the intensity profiles of PCOADVBs are related to the topological charges M_1 and M_2, and the ring intensity pattern of a PCOADVB can be destroyed when $M_1 > M_2$ at $z = 10$ m (Figure 4a). As z increases to $z = 80$ m, the intensity of a PCOADVB with $M_1 = 2$ and $M_2 = 1$ also evolves into one spot (Figure 4b). When $M_1 < M_2$ (Figure 5), the intensity profile of a PCOADVB with $M_1 = 1$ and $M_2 = 2$ has an elliptical ring profile accompanied by a bright spot on the right. Furthermore, the intensity profile of a PCOADVB with $M_1 = 1$ and $M_2 = 2$ can also become one spot pattern at $z = 80$ m (Figure 5b). Comparing Figure 4 with Figure 5, one concludes that the intensity profiles of PCOADVB are controlled by setting the topological charges M_1 and M_2 at a short distance, and the intensity pattern of a PCOADVB with different M_1 and M_2 can all evolve from an elliptical ring pattern into one spot pattern. From Figures 1, 3 and 5, one finds that the intensity profile of PCOADVBs is determined by off-axis positions and topological charges.

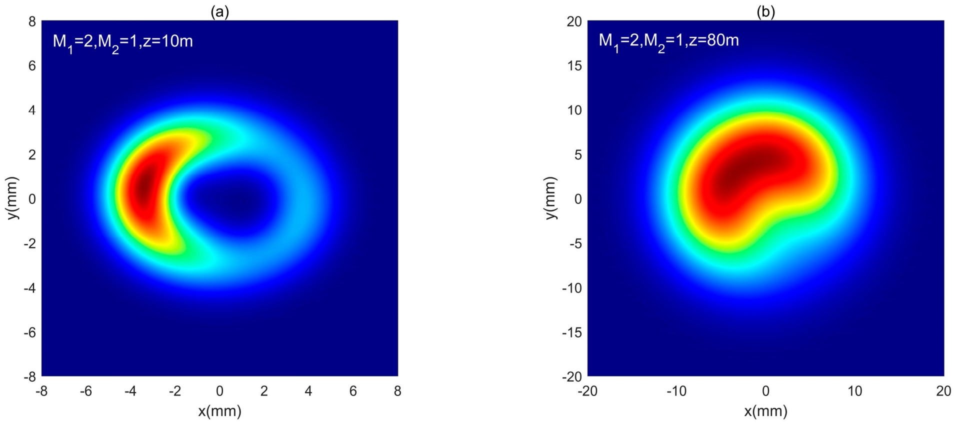

Figure 4. The intensity of a PCOADVB with $M_1 = 2$ and $M_2 = 1$ in free space. (**a**) $z = 10$ m, and (**b**) $z = 80$ m.

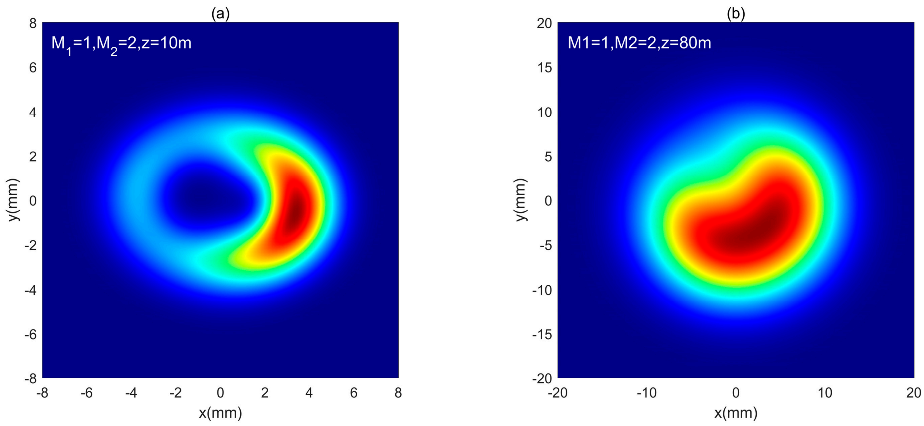

Figure 5. The intensity of a PCOADVB with $M_1 = 1$ and $M_2 = 2$ in free space. (**a**) $z = 10$ m, (**b**) $z = 80$ m.

From the above analysis, it was found that the spot pattern of a PCOADVB in free space can be obtained on propagation. To view the effects of σ on the evolution of the intensity profiles of a PCOADVB, Figure 6 illustrates the intensity profile of a PCOADVB with $(x_{1d}, y_{1d}) = (1\text{ mm}, 0)$ and $(x_{2d}, y_{2d}) = (-1\text{ mm}, 0)$ for different values of σ. In Figure 6a, when the σ decreases to $\sigma = 1.5$ mm, the intensity profile of a PCOADVB in free space becomes one spot pattern at $z = 40$ m, while the intensity profile of a PCOADVB with $\sigma = 2$ mm at $z = 40$ m evolves into a spot pattern with two peaks (Figure 3b). As z increases to $z = 80$ m, the PCOADVB with $\sigma = 1.5$ mm becomes one spot pattern with a Gaussian-like profile (Figure 6b). Thus, the PCOADVB with a smaller σ can evolve into one spot pattern faster (comparing Figure 3b with Figure 6a). On the other hand, when the σ increases to $\sigma = 2.5$ mm, the intensity profile of a PCOADVB can have one spot pattern with two peaks at $z = 40$ m (Figure 6c), and this intensity pattern will remain at $z = 80$ m (Figure 6d). Hence, the intensity profile of a PCOADVB with a larger σ will evolve into a spot pattern more slowly, while the intensity profiles of a PCOADVB with $\sigma = 2$ mm or $\sigma = 1.5$ mm can all become one spot at $z = 80$ m. From the above analysis, one concludes that a smaller σ will accelerate the PCOADVB's evolution into one spot and become one spot with a Gaussian-like profile at a short distance.

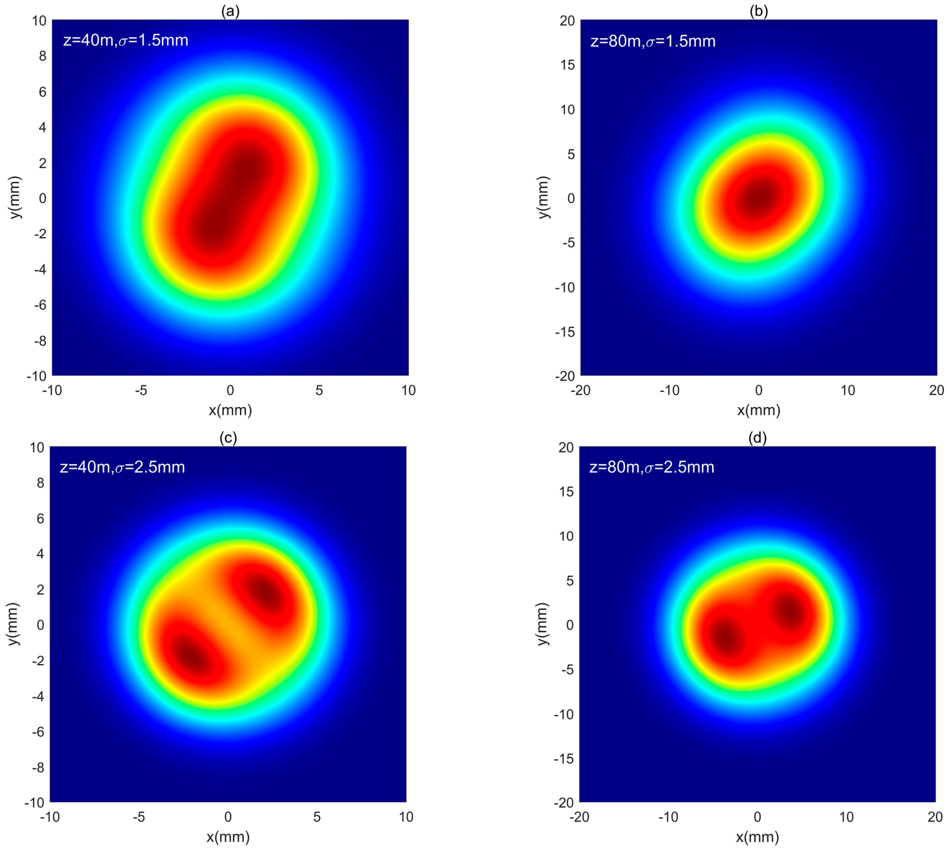

Figure 6. The intensity of a PCOADVB for the different σ in free space.

When the PCOADVB propagates through a turbulent ocean, the intensity profiles of a PCOADVB can be affected by oceanic turbulence. The intensity profiles of a PCOADVB with $(x_{1d}, y_{1d}) = (1\text{ mm}, 0)$, $(x_{2d}, y_{2d}) = (0, 1\text{ mm})$, and $\sigma = 2$ mm in oceanic turbulence are shown in Figures 7 and 8. In Figure 7a, the intensity profile of a PCOADVB in oceanic turbulence remains an off-axis ring intensity pattern at $z = 10$ m, but the hollow area is smaller than the same beam in free space (Figure 1a). As z increases further, the intensity pattern of a PCOADVB in oceanic turbulence loses its off-axis intensity profile and becomes a spot at $z = 40$ m (Figure 7b). As z increases to $z = 80$ m, the intensity profile of a PCOADVB in oceanic turbulence becomes one spot with a Gaussian-like profile (Figure 7c), while this PCOADVB in free space becomes just one spot (Figure 1c). From the above analysis, one can see that the intensity profile of a PCOADVB in oceanic turbulence can evolve into one spot with a Gaussian-like profile faster than the same beam in free space. As z increases further, the beam spot with the Gaussian-like profile of a PCOADVB will spread further (Figure 7d), while the same beam in free space has an off-axis Gaussian-like pattern (Figure 1d). The observation that the PCOADVB evolves into a Gaussian-like spot more rapidly is due to the effects of oceanic turbulence. The strength of oceanic turbulence is determined by the oceanic turbulence parameters x_T, ε, and ς, and the strong oceanic turbulence can be realized when x_T is larger. In this work, only the influences of x_T on intensity profiles of a PCOADVB are investigated. Figure 8 shows the intensity profile of a PCOADVB in oceanic turbulence with $x_T = 10^{-6}$ K^2/s. In Figure 8a, the intensity of a PCOADVB almost loses the ring pattern, while the beam in oceanic turbulence with $x_T = 10^{-7}$ K^2/s maintains an off-axis ring pattern (Figure 7a). As z increases to $z = 40$ m, the intensity profile of this PCOADVB becomes a Gaussian-like pattern (Figure 7b). Moreover, the same PCOADVB in oceanic turbulence with $x_T = 10^{-7}$ K^2/s becomes an off-axis spot at $z = 40$ m (Figure 7b). Figure 9 illustrates the intensity profiles of a PCOADVB with $(x_{1d}, y_{1d}) = (1\text{ mm}, 0)$, $(x_{2d}, y_{2d}) = (-1\text{ mm}, 0)$, and $\sigma = 2$ mm in oceanic turbulence with $x_T = 10^{-7}$ K^2/s. The intensity of a PCOADVB loses the ring pattern and evolves into a spot with a Gaussian-like pattern (comparing Figure 3a with Figure 9b), while the intensity profile of the same beam in free space becomes just one spot (Figure 3c). Thus, the PCOADVB in oceanic turbulence easily transforms into a Gaussian-like profile. One can conclude that the intensity profile of a PCOADVB in stronger oceanic turbulence (larger x_T) will evolve into a spot with a Gaussian-like pattern more rapidly, and the PCOADVB may have applications in underwater laser detection and wireless communications.

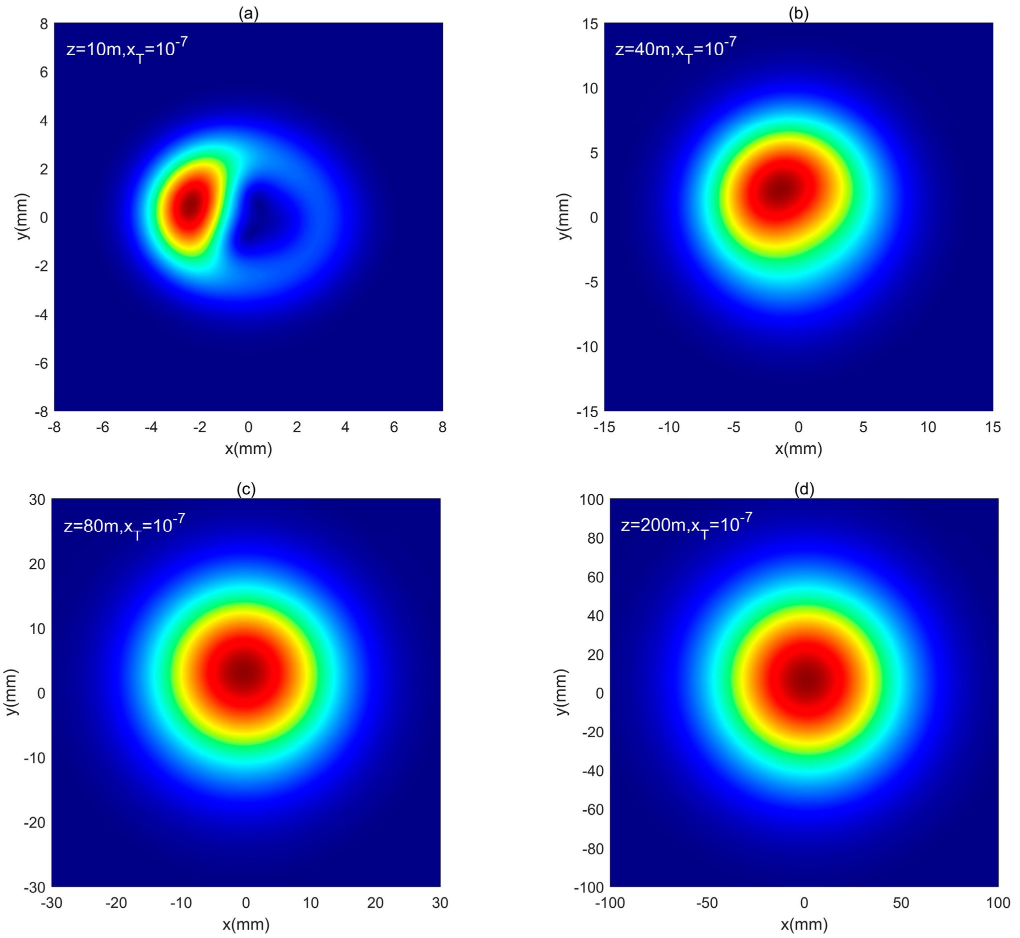

Figure 7. The intensity of a PCOADVB in oceanic turbulence. (**a**) $z = 10$ m, (**b**) $z = 40$ m, (**c**) $z = 80$ m, and (**d**) $z = 200$ m.

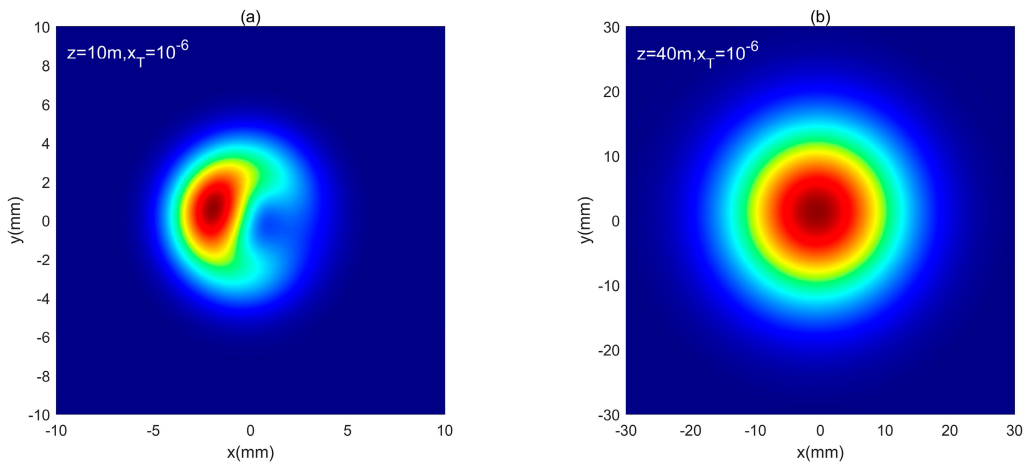

Figure 8. The intensity of a PCOADVB in oceanic turbulence with $x_T = 10^{-6}$. (**a**) $z = 10$ m, and (**b**) $z = 40$ m.

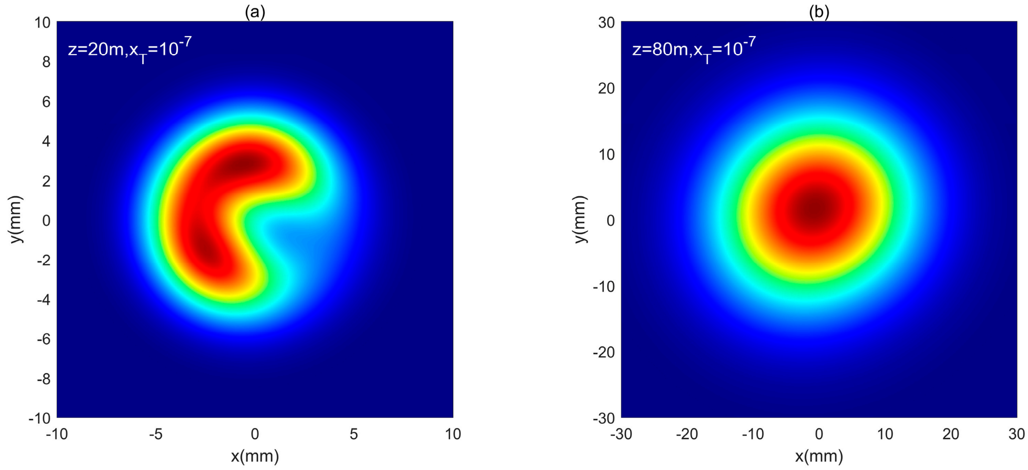

Figure 9. The intensity of a PCOADVB in oceanic turbulence with $x_T = 10^{-7}$. (**a**) $z = 20$ m, and (**b**) $z = 80$ m.

The evolution of coherence vortices of a PCOADVB with $(x_{1d}, y_{1d}) = (1\text{ mm}, 0)$, $(x_{2d}, y_{2d}) = (0, 1\text{ mm})$, and $\sigma = 2$ mm is illustrated in Figures 10 and 11. The lines of $\mathrm{Re}[\mu(\boldsymbol{\rho}_1, \boldsymbol{\rho}_2, z)] = 0$ and $\mathrm{Im}[\mu(\boldsymbol{\rho}_1, \boldsymbol{\rho}_2, z)] = 0$ for a PCOADVB with $M_1 = M_2 = 1$ in free space are plotted in Figure 10. The number of coherence vortices of a PCOADVB with $M_1 = M_2 = 1$ in free space maintains two coherence vortices at $z = 10$ m (Figure 10a). As z increases to $z = 80$ m, the number of coherence vortices of such a beam remains unchanged (Figure 10b). Comparing Figure 10a with Figure 10b, the positions of the coherence vortices move as z increases. Figure 11 shows the lines of $\mathrm{Re}[\mu(\boldsymbol{\rho}_1, \boldsymbol{\rho}_2, z)] = 0$ and $\mathrm{Im}[\mu(\boldsymbol{\rho}_1, \boldsymbol{\rho}_2, z)] = 0$ for a PCOADVB with $M_1 = M_2 = 1$ in oceanic turbulence. From Figure 11a, one can see that the number of coherence vortices of a PCOADVB in oceanic turbulence increases. As z increases, the position of coherence also changes (Figure 11b). In a previous work, the number of coherence vortices for a beam array in atmospheric turbulence also changes [41]. In addition, the observation that the number of coherence vortices in oceanic turbulence changes is the same as the results of previous studies involving vortex beams [42].

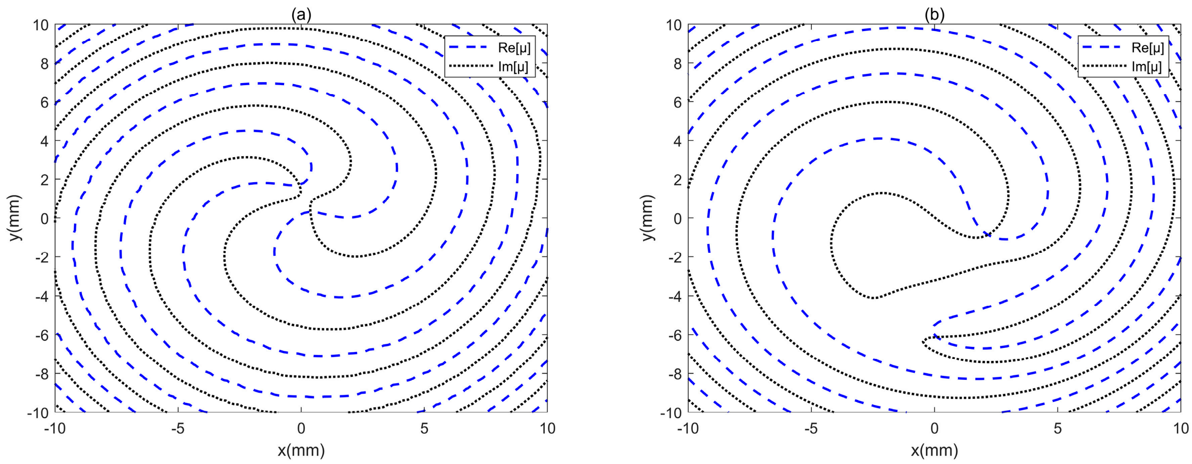

Figure 10. Lines of $\mathrm{Re}[\mu(\boldsymbol{\rho}_1, \boldsymbol{\rho}_2, z)] = 0$ and $\mathrm{Im}[\mu(\boldsymbol{\rho}_1, \boldsymbol{\rho}_2, z)] = 0$ for a PCOADVB in free space. (**a**) $z = 10$ m and (**b**) $z = 80$ m.

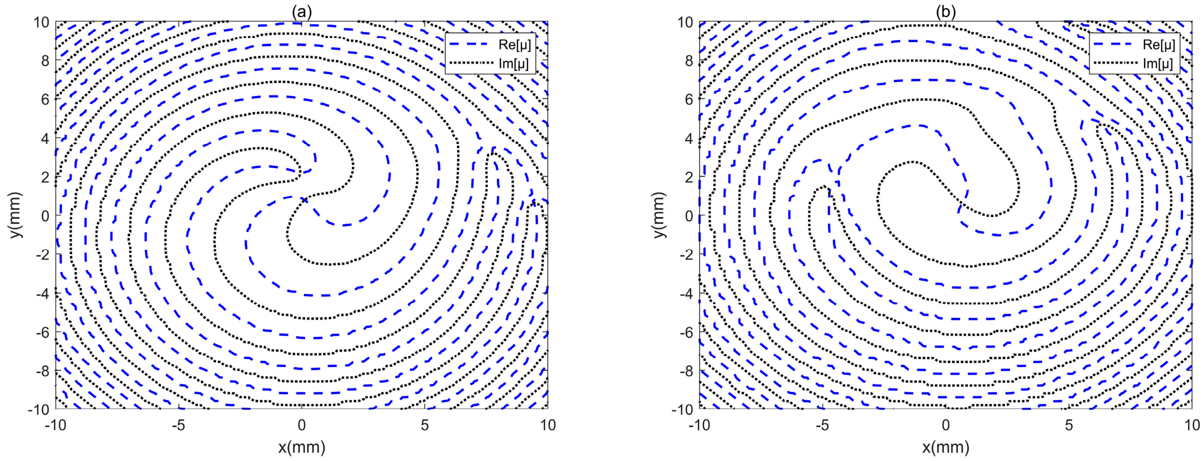

Figure 11. Lines of $\mathrm{Re}[\mu(\boldsymbol{\rho}_1, \boldsymbol{\rho}_2, z)] = 0$ and $\mathrm{Im}[\mu(\boldsymbol{\rho}_1, \boldsymbol{\rho}_2, z)] = 0$ for a PCOADVB in oceanic turbulence. (**a**) $z = 10$ m and (**b**) $z = 80$ m.

5. Conclusions

In this work, a new type of beam called a PCOADVB with two off-axis vortices correlated with a GSM source was introduced, and the analytical CSD of a PCOADVB in a turbulent ocean was derived based on the Huygens–Fresnel theory. Based on the derived CSD, the relationships between the initial source parameters and oceanic turbulence with the intensity profiles of the PCOADVBs were discussed. It was found that the intensity profiles of a PCOADVB in free space have an off-axis ring intensity profile at a short distance, and the intensity of a PCOADVB gradually loses its off-axis ring pattern and evolves into a spot with a Gaussian-like profile on propagation. Furthermore, the OADVB in free space maintains its off-axis intensity pattern at longer values of z. The smaller coherence length helps the PCOADVB evolve into a spot with a Gaussian-like profile as z increases. The intensity pattern of a PCOADVB at a short distance can be controlled by setting the source parameters M_1, M_2, (x_{1d}, y_{1d}), and (x_{2d}, y_{2d}); the differences in the intensity profiles of PCOADVBs for the different initial parameters gradually disappear, and the PCOADVB evolves to become a single spot with a Gaussian-like profile as z increases. The observation that the PCOADVB evolves into one spot in free space is caused by coherence length. The intensity of a PCOADVB in oceanic turbulence will gradually lose its off-axis intensity profile and become a spot with a Gaussian profile more rapidly. Moreover, the stronger oceanic turbulence will accelerate the evolution of the PCOADVB into a Gaussian-like profile at a short z. The results also show that the number of coherence vortices of a PCOADVB in free space remains unchanged, while the positions of the coherence vortices will move on propagation. However, the number and positions of the coherence vortices of the same PCOADVB in oceanic turbulence will change as z increases. These results may have applications in underwater laser sensing and wireless communications.

Author Contributions: Conceptualization, D.L.; writing—original draft preparation, L.C. and Y.Y.; writing—review and editing, G.W. and D.L.; software, Y.W.; data curation, H.Z. and L.C.; project administration, G.W. and D.L. All authors have read and agreed to the published version of the manuscript.

Funding: This work was supported by the National Natural Science Foundation of China (11604038, 11875096, and 11404048).

Institutional Review Board Statement: Not applicable.

Informed Consent Statement: Not applicable.

Data Availability Statement: The data presented in this work are available upon request from the corresponding author.

Conflicts of Interest: The authors declare no conflicts of interest.

References

1. Baykal, Y.; Ata, Y.; Gökçe, M.C. Underwater turbulence, its effects on optical wireless communication and imaging: A review. *Opt. Laser Technol.* **2022**, *156*, 108624. [CrossRef]
2. Nikishov, V.V.; Nikishov, V.I. Spectrum of Turbulent Fluctuations of the Sea-Water Refraction Index. *Int. J. Fluid Mech. Res.* **2000**, *27*, 82–98. [CrossRef]
3. Li, Y.; Zhang, Y.; Zhu, Y. Oceanic spectrum of unstable stratification turbulence with outer scale and scintillation index of Gaussian-beam wave. *Opt. Express* **2019**, *27*, 7656–7672. [CrossRef]
4. Yao, J.R.; Elamassie, M.; Korotkova, O. Spatial power spectrum of natural water turbulence with any average temperature, salinity concentration, and light wavelength. *J. Opt. Soc. Am. A* **2020**, *37*, 1614–1621. [CrossRef] [PubMed]
5. Farwell, N.; Korotkova, O. Intensity and coherence properties of light in oceanic turbulence. *Opt. Commun.* **2012**, *285*, 872–875. [CrossRef]
6. Korotkova, O.; Farwell, N. Effect of oceanic turbulence on polarization of stochastic beams. *Opt. Commun.* **2011**, *284*, 1740–1746. [CrossRef]
7. Korotkova, O.; Farwell, N.; Shchepakina, E. Light scintillation in oceanic turbulence. *Wave Random Complex.* **2012**, *22*, 260–266. [CrossRef]
8. Baykal, Y. Scintillation index in strong oceanic turbulence. *Opt. Commun.* **2016**, *375*, 15–18. [CrossRef]
9. Wang, Z.; Zhang, P.; Qiao, C.; Lu, L.; Fan, C.; Ji, X. Scintillation index of Gaussian waves in weak turbulent ocean. *Opt. Commun.* **2016**, *380*, 79–86. [CrossRef]
10. Yousefi, M.; Kashani, F.D.; Golmohammady, S.; Mashal, A. Scintillation and bit error rate analysis of a phase-locked partially coherent flat-topped array laser beam in oceanic turbulence. *J. Opt. Soc. Am. A Opt. Image Sci. Vis.* **2017**, *34*, 2126–2137. [CrossRef]
11. Ata, Y.; Yao, J.; Korotkova, O. BER variation of an optical wireless communication system in underwater turbulent medium with any temperature and salinity concentration. *Opt. Commun.* **2021**, *485*, 126751. [CrossRef]
12. Ata, Y. Structure function, coherence length, and angle-of-arrival variance for Gaussian beam propagation in turbulent waters. *J. Opt. Soc. Am. A Opt. Image Sci. Vis.* **2022**, *39*, 63–71. [CrossRef]
13. Liu, D.J.; Wang, Y.C.; Wang, G.Q.; Yin, H.M.; Wang, J.R. The influence of oceanic turbulence on the spectral properties of chirped Gaussian pulsed beam. *Opt. Laser Technol.* **2016**, *82*, 76–81. [CrossRef]
14. Jo, J.-H.; Ri, O.-H.; Ju, T.Y.; Pak, K.-M.; Ri, S.-G.; Hong, K.-C.; Hyon Jang, S. Effect of oceanic turbulence on the spectral changes of diffracted chirped Gaussian pulsed beam. *Opt. Laser Technol.* **2022**, *153*, 108200. [CrossRef]
15. Wang, F.; Liu, X.L.; Cai, Y.J. Propagation of Partially Coherent Beam in Turbulent Atmosphere: A Review. *Prog. Electromagn. Res.* **2015**, *150*, 123–143. [CrossRef]
16. Wu, Y.Q.; Zhang, Y.X.; Li, Y.; Hu, Z.D. Beam wander of Gaussian-Schell model beams propagating through oceanic turbulence. *Opt. Commun.* **2016**, *371*, 59–66. [CrossRef]
17. Lu, C.; Zhao, D. Statistical properties of rectangular cusped random beams propagating in oceanic turbulence. *Appl. Opt.* **2017**, *56*, 6572–6576. [CrossRef]
18. Chen, X.D.; Zhao, D.M. Propagation properties of electromagnetic rectangular multi-Gaussian Schell-model beams in oceanic turbulence. *Opt. Commun.* **2016**, *372*, 137–143. [CrossRef]
19. Liu, X.; Zhou, G.; Shen, Y. Effect of oceanic turbulence with anisotropy on the propagation of multi-sinc Schell-model beams. *Results Phys.* **2022**, *36*, 105447. [CrossRef]
20. Liu, Y.; Zhao, Y.; Liu, X.; Liang, C.; Liu, L.; Wang, F.; Cai, Y. Statistical Characteristics of a Twisted Anisotropic Gaussian Schell-Model Beam in Turbulent Ocean. *Photonics* **2020**, *7*, 37. [CrossRef]
21. Liu, L.; Liu, Y.; Chang, H.; Huang, J.; Zhu, X.; Cai, Y.; Yu, J. Second-Order Statistics of Self-Splitting Structured Beams in Oceanic Turbulence. *Photonics* **2023**, *10*, 339. [CrossRef]
22. Luo, B.; Wu, G.H.; Yin, L.F.; Gui, Z.C.; Tian, Y.H. Propagation of optical coherence lattices in oceanic turbulence. *Opt. Commun.* **2018**, *425*, 80–84. [CrossRef]
23. Ye, F.; Xie, J.; Hong, S.; Zhang, J.; Deng, D. Propagation properties of a controllable rotating elliptical Gaussian optical coherence lattice in oceanic turbulence. *Results Phys.* **2019**, *13*, 102249. [CrossRef]
24. Liu, D.; Zhong, H.; Wang, G.; Yin, H.; Wang, Y. Radial phased-locked multi-Gaussian Schell-model beam array and its properties in oceanic turbulence. *Opt. Laser Technol.* **2020**, *124*, 106003. [CrossRef]
25. Huang, Y.P.; Zhang, B.; Gao, Z.H.; Zhao, G.P.; Duan, Z.C. Evolution behavior of Gaussian Schell-model vortex beams propagating through oceanic turbulence. *Opt. Express* **2014**, *22*, 17723–17734. [CrossRef] [PubMed]
26. Liu, D.; Wang, G.; Yin, H.; Zhong, H.; Wang, Y. Propagation properties of a partially coherent anomalous hollow vortex beam in underwater oceanic turbulence. *Opt. Commun.* **2019**, *437*, 346–354. [CrossRef]
27. Wang, X.; Wang, L.; Zhao, S. Propagation Properties of an Off-Axis Hollow Gaussian-Schell Model Vortex Beam in Anisotropic Oceanic Turbulence. *J. Mar. Sci. Eng.* **2021**, *9*, 1139. [CrossRef]
28. Fang, G.J.; Pu, J.X. Propagation properties of stochastic electromagnetic double-vortex beams in a turbulent atmosphere. *Chin. Phys. B* **2012**, *21*, 084203. [CrossRef]
29. Fang, G.J.; Sun, S.H.; Pu, J.X. Experimental study on fractional double-vortex beams. *Acta Phys. Sin.-Ch. Ed.* **2012**, *61*, 064210. [CrossRef]

30. Liu, Y.; Zhang, K.; Chen, Z.; Pu, J. Scintillation index of double vortex beams in turbulent atmosphere. *Optik* **2019**, *181*, 571–574. [CrossRef]
31. Du, Y.; Liu, D.; Fu, S.; Wang, Y.; Qin, Y. Reconfigurable generation of double-ring perfect vortex beam. *Opt. Express* **2021**, *29*, 17353–17364. [CrossRef] [PubMed]
32. Rickenstorff, C.; Gomez-Pavon, L.D.C.; Sosa-Sanchez, C.T.; Silva-Ortigoza, G. Paraxial and tightly focused behaviour of the double ring perfect optical vortex. *Opt. Express* **2020**, *28*, 28713–28726. [CrossRef] [PubMed]
33. Ke, X.Z.; Zhang, L. Study on orthogonal superposition generation method of double-ring vortex beams. *Eur. Phys. J. D* **2020**, *74*, 45. [CrossRef]
34. Guo, M.; Le, W.; Wang, C.; Rui, G.; Zhu, Z.; He, J.; Gu, B. Generation, Topological Charge, and Orbital Angular Momentum of Off-Axis Double Vortex Beams. *Photonics* **2023**, *10*, 368. [CrossRef]
35. Honari-Latifpour, M.; Ding, J.; Barbuto, M.; Takei, S.; Miri, M.A. Self-Organized Vortex and Antivortex Patterns in Laser Arrays. *Phys. Rev. Appl.* **2021**, *16*, 054010. [CrossRef]
36. Li, Q.; Wu, C.; Zhang, Z.H.; Zhao, S.; Zhong, B.; Li, S.; Li, H.Q.; Jin, L.J. High-Purity Multi-Mode Vortex Beam Generation With Full Complex-Amplitude-Controllable Metasurface. *IEEE Trans. Antennas Propag.* **2023**, *71*, 774–782. [CrossRef]
37. Barbuto, M.; Alù, A.; Bilotti, F.; Toscano, A. Composite Vortex Manipulation as a Design Tool for Reflective Intelligent Surfaces. *IEEE Antennas Wirel. Propag. Lett.* **2023**, *22*, 2392–2396. [CrossRef]
38. Wolf, E. Unified theory of coherence and polarization of random electromagnetic beams. *Phys. Lett. A* **2003**, *312*, 263–267. [CrossRef]
39. Jeffrey, A.; Dai, H.H. *Handbook of Mathematical Formulas and Integrals*, 4th ed.; Academic Press Inc.: Cambridge, MA, USA, 2008.
40. Gbur, G.; Visser, T.D. Coherence vortices in partially coherent beams. *Opt. Commun.* **2003**, *222*, 117–125. [CrossRef]
41. Li, J.H.; Zhang, H.R.; Lu, B.D. Composite coherence vortices in a radial beam array propagating through atmospheric turbulence along a slant path. *J. Opt.* **2010**, *12*, 065401. [CrossRef]
42. Liu, D.; Yin, H.; Wang, G.; Wang, Y. Propagation of partially coherent Lorentz–Gauss vortex beam through oceanic turbulence. *Appl. Opt.* **2017**, *56*, 8785–8792. [CrossRef] [PubMed]